Journal of The Electrochemical Society, **154** (8) B823-B834 (2007)
0013-4651/2007/154(8)/B823/12/$20.00 © The Electrochemical Society

Anisotropic Heat and Water Transport in a PEFC Cathode Gas Diffusion Layer

Ugur Pasaogullari,[a,z] Partha P. Mukherjee,[b,*] Chao-Yang Wang,[b,] and Ken S. Chen[c,**]**

[a]*Connecticut Global Fuel Cell Center and Department of Mechanical Engineering, University of Connecticut, Storrs, Connecticut 06269-5233, USA*
[b]*Electrochemical Engine Center and Department of Mechanical and Nuclear Engineering, The Pennsylvania State University, University Park, Pennsylvania 16802, USA*
[c]*Engineering Sciences Center, Sandia National Laboratories, Albuquerque, New Mexico 87185-0836, USA*

A nonisothermal, two-phase model was developed to investigate simultaneous heat and mass transfer in the cathode gas diffusion layer (GDL) of a polymer electrolyte fuel cell (PEFC). The model was applied in two-dimensions with the in-plane (i.e., channel-to-land) and through-plane (i.e., catalyst layer-to-channel) directions to investigate the effects of anisotropy of GDL. For the first time, the anisotropy in the GDL properties was taken into account and found to be an important factor controlling the temperature distribution in the GDL. The maximum temperature difference in the GDL was found to be a strong function of GDL anisotropy. A temperature difference of up to 5°C at a cell voltage of 0.4 V was predicted for an isotropic GDL while it reduced to 3°C for an anisotropic GDL. Significant effect of temperature distribution on liquid water transport and distribution was also observed. In addition, the latent heat effects due to condensation/evaporation of water on the temperature and water distributions were analyzed and found to strongly affect the two-phase transport.
 [DOI: 10.1149/1.2745714]

Manuscript submitted November 9, 2006; revised manuscript received April 10, 2007. Available electronically June 15, 2007.

Polymer electrolyte fuel cells (PEFCs), owing to their high energy efficiency, low emission, and low noise, are widely considered as the most promising alternative power source in the 21st century for automotive, portable, and stationary applications. A typical PEFC consists of several distinct components: the membrane electrode assembly (MEA) comprising a proton conducting electrolyte membrane sandwiched between two catalyst layers (CL), the porous gas diffusion layers (GDL), and the bipolar plates with embedded gas channels. In the anode CL, the hydrogen oxidation reaction (HOR) splits the hydrogen into electrons, which are transmitted via the external circuit, and protons, which migrate through the membrane and participate in the oxygen reduction reaction (ORR) in the cathode CL to recombine with oxygen and producing water and waste heat.

Despite significant progress in recent years in enhancing the overall cell performance, a major limitation arises from the two-phase transport. This is primarily owing to the blockage of the open pore paths due to liquid water in the cathode GDL, thus hindering oxygen transport to the active reaction sites in the CL. GDL plays a crucial role in the overall water management, which requires a delicate balance between reactant transport from the gas channels and water removal from the electrochemically active sites. Effective water management prevents flooding while ensuring sufficient membrane hydration to minimize ohmic losses. Along with water management, thermal management is also a key to high performance and longevity of PEFCs. At an energy-conversion efficiency of roughly 50%, a PEFC produces nearly the same amount of waste heat as it does electric power output. Furthermore, PEFCs tolerate only a small temperature variation, less than 5°C (Wang[1] and Ju et al.[2]). This is primarily because the proton conductivity of the polymer electrolyte membrane strongly depends on the degree of its hydration and, hence, on the membrane temperature because the vapor saturation pressure is a strong function of temperature, as shown in Fig. 1. It is seen that 5°C temperature difference brings about 23% in the vapor saturation pressure and, hence, water activity. Additionally, condensation of water vapor releases heat, causing undesirable local hot spots, which could reduce the membrane performance by reducing the degree of hydration and, hence, accelerate degradation. These concerns require rigorous thermal management in a PEFC, coupled with precise water management. Thus, fundamental understanding of thermal transport phenomena is of paramount importance and the nonisothermal two-phase PEFC model presented here is extremely useful for elucidating heat-transfer mechanisms and quantify the temperature distribution.

Several studies[3-9] have attempted to predict temperature distribution under single-phase (dry) conditions in a PEFC. Most recently, Wang[1] and Ju et al.[2] reviewed the single-phase, nonisothermal models of PEFCs in detail.

Two-phase transport in PEFCs has been studied by several researchers[10-20] in varied levels of complexities; however, the focus of these studies was primarily on the isothermal investigation of the transport phenomena. The issue of two-phase heat-transfer with condensation/evaporation, leading toward a simultaneous description of water and thermal management, has hardly been explored. In their works, Nam and Kaviany,[21] and Rowe and Li[22] both studied the phenomena using a one-dimensional model. Nam and Kaviany[21]

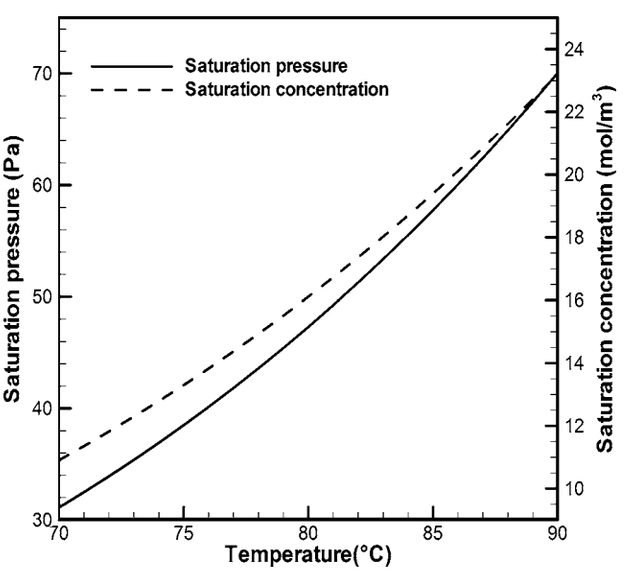

Figure 1. Dependence of the water saturation pressure on temperature in the typical PEFC operating temperature range.

* Electrochemical Society Student Member.
** Electrochemical Society Active Member.
z E-mail: ugur.pasaogullari@uconn.edu

focused on the two-phase transport in the cathode GDL of a PEFC with particular emphasis on the influence of the GDL structure, in terms of fiber diameter, porosity, and capillary pressure, on the water removal rate. On the other hand, the model of Rowe and Li[22] was more rigorous, and included a comprehensive description of multicomponent species (oxygen, hydrogen, and vapor/liquid water) transport as well as proton and electron transport.

Among the multidimensional, nonisothermal, two-phase models for a PEFC, notable works include Yuan and Sunden,[23] Costamagna,[24] Berning and Djilali,[25] Mazumder and Cole,[26] and Bradean et al.[27] Except for Costamagna,[24] all of the afore-mentioned multidimensional models considered the phase change effect. In contrast to the two-phase model of Berning and Djilali[25] based on the unsaturated flow theory (UFT) with the assumption of constant gas pressure across the porous medium, Mazumder and Cole[26] adopted the multiphase mixture (M^2) model originally developed by Wang and Cheng.[28] Birgersson et al.[29] and Senn and Poulikakos[30] recently presented a two-dimensional, nonisothermal, two-phase model based on the multifluid approach, which is in contrast to the M^2 model approach. Birgersson et al. further emphasized the importance of thermal contact resistance on the flooding behavior. Most recently, Wang and Wang[31] developed a full-cell, nonisothermal, two-phase model based on the M^2 approach and identified the importance of water transport as well as heat removal via vapor-phase diffusion under the temperature gradient. However, none of the prior models took into account the effect of intrinsic anisotropy in the GDL structure on the two-phase heat transport phenomena.

Unlike the typical porous media often encountered in reservoir simulations or groundwater flows, the GDL structure is characterized by a fibrous porous medium, exhibiting significant anisotropy due to the orientation of the underlying fibers as shown in Fig. 2 for a typical carbon paper GDL. Due to the preferential orientation of the constituting fibers, the GDL exhibits strong anisotropy leading to different transport coefficients in the through-plane and in-plane directions. In the present work, two-phase heat-transfer and temperature distribution in a PEFC cathode GDL was analyzed in detail, with particular emphasis on the effect of GDL anisotropy on the underlying heat and water transport. Therefore, the primary objective of this work was to present a model for predicting two-phase flow and thermal transport and the underlying interactions occurring in the cathode GDL of a PEFC.

Mathematical Model

In the present study, we focused on two-phase transport of water and heat in the cathode GDL of a PEFC; accordingly, the modeling domain was limited to cathode GDL only, and the boundary conditions were specified at the interfaces of GDL with catalyst layer, gas channel, and current collector, as shown schematically in Fig. 3a. The associated transport fluxes are shown in Fig. 3b. Taking advantage of the symmetries of the configuration, the two-dimensional cross section of the GDL (Fig. 3a, the rectangle ABCDE) between the catalyst layer and half of the channel and half of the current-collector land is considered.

Two-phase model and governing equations.— Our model is based on the multiphase mixture model (M^2), originally proposed by Wang and Cheng[28] and used later for two-phase PEFC modeling by Wang et al.,[10] You and Liu,[12] Pasaogullari et al.,[15-18] Meng and Wang,[20] Mazumder and Cole,[26] and Wang and Wang.[31] The multiphase mixture (M^2) model is an exact reformulation of the classical two-fluid, two-phase model in a single equation. One salient feature of the M^2 model is that it can be conveniently used in a computational domain where single- and two-phase zones coexist, which is often the case in a PEFC. In classical two-fluid models, the interface between single- and two-phase zones must be tracked explicitly, which substantially increases the numerical complexity.

Mass conservation.— Mass conservation for the two-phase mixture as given by the M^2 model is

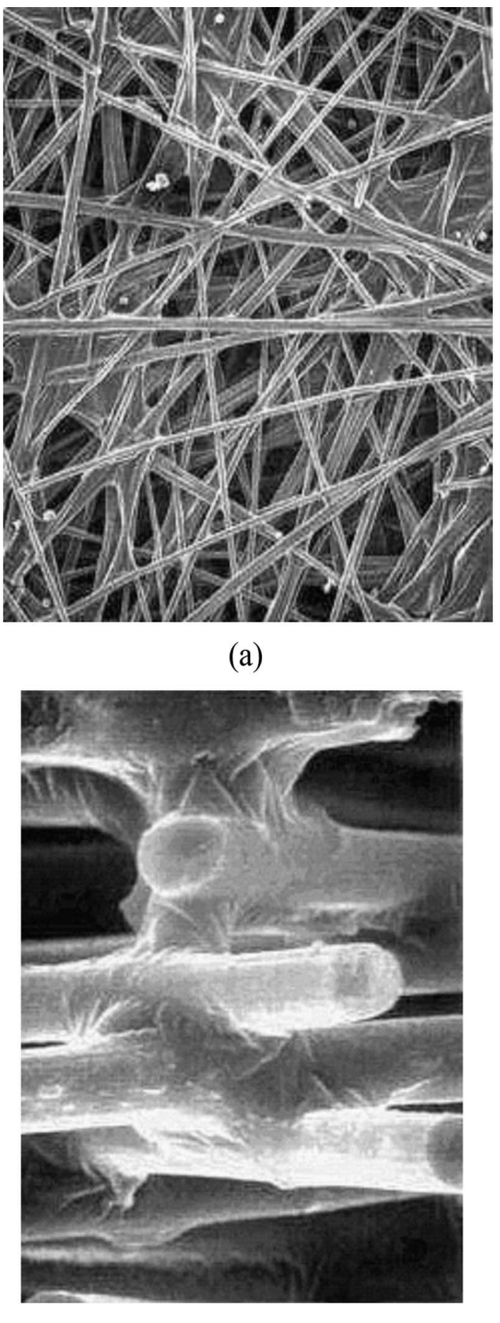

Figure 2. SEM images of a Toray TGPH series carbon paper GDL. (a) Surface and (b) cross section.[37]

$$\frac{\partial(\varepsilon\rho)}{\partial t} + \nabla \cdot (\rho \mathbf{u}) = 0 \quad [1]$$

where, $\mathbf{u}$ and ρ are the superficial mixture velocity and mixture density, respectively[28]

$$\rho = \rho_l s + \rho_g (1 - s) \quad [2]$$

Here, s and $(1 - s)$ represent the fraction of the open pore space occupied by the liquid and gas phases, respectively.

Momentum conservation.— The momentum conservation for the two-phase mixture based on the mixture velocity $\mathbf{u}$ is

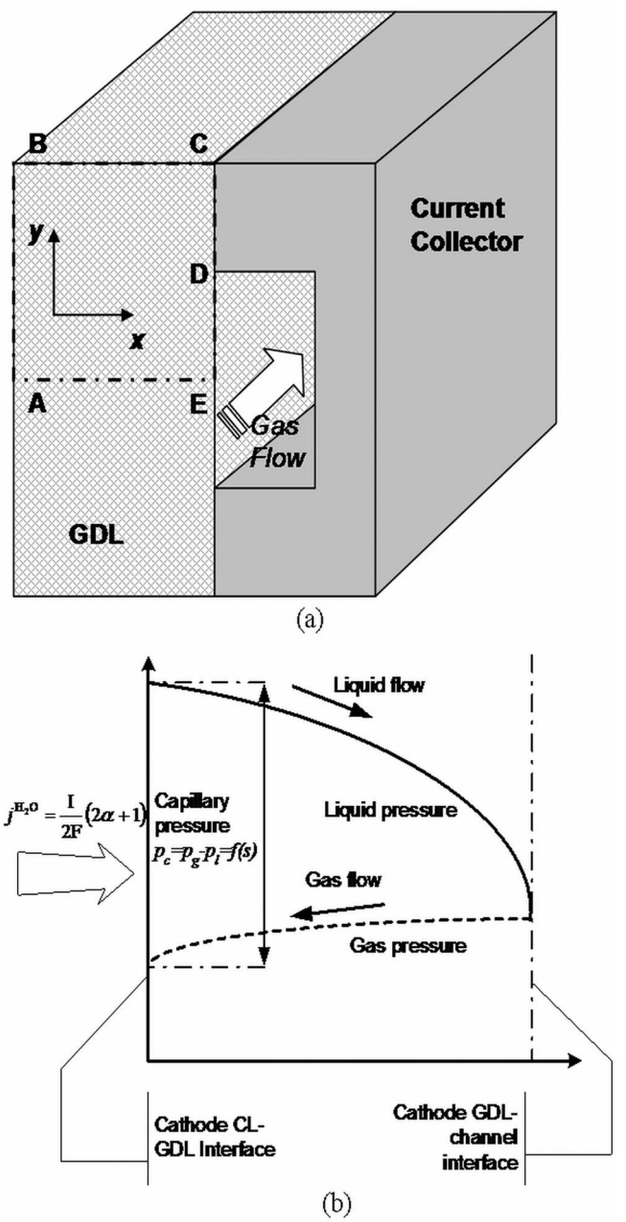

Figure 3. Schematic diagrams of (a) modeling domain and (b) transport processes and phase pressures in the GDL.

$$\frac{1}{\varepsilon}\left[\frac{\partial(\rho\mathbf{u})}{\partial t} + \frac{1}{\varepsilon}\nabla\cdot(\rho\mathbf{u}\mathbf{u})\right] = \nabla\cdot(\mu\nabla\mathbf{u}) - \nabla p - \frac{\mu}{K}\mathbf{u} \quad [3]$$

where, μ is the mixture viscosity[28]

$$\mu = \rho\left[\frac{k_{rl}}{\nu_l} + \frac{k_{rg}}{\nu_g}\right]^{-1} \quad [4]$$

Equation 3 is the Brinkman extension to Darcy's law using superficial velocities (i.e., based on total volume, rather than the open pore volume); therefore the predicted velocities are continuous at interfaces.

Species conservation.— The species conservation equation in the M^2 model, written in terms of molar concentration, is[16]

$$\frac{\partial(C^i)}{\partial t} + \nabla\cdot(\gamma_c\mathbf{u}C^i) = \nabla\cdot[\mathbf{D}_g^{i,\text{eff}}\nabla C_g^i] - \nabla\cdot\left[\left(\frac{C_l^i}{\rho_l} - \frac{C_g^i}{\rho_g}\right)\mathbf{j}_l\right] \quad [5]$$

where C^i is the total concentration of species i in liquid and gas phases. The liquid and gas phase have different flow-fields; therefore the advective transport of species is corrected via an advection correction factor, γ_c

$$\gamma_c = \begin{cases} \dfrac{\rho}{C^{H_2O}}\left(\dfrac{\lambda_l}{M^{H_2O}} + \lambda_g\dfrac{C_g^{H_2O}}{\rho_g}\right) & \text{for water} \\ \dfrac{\rho\lambda_g}{\rho_g(1-s)} & \text{for other species} \end{cases} \quad [6]$$

where λ_l and λ_g are the relative mobility of liquid and gas phases, respectively

$$\lambda_k = \frac{k_{rk}/\nu_k}{\sum_k k_{rk}/\nu_k} \quad [7]$$

where k_{rl} and k_{rg} are the relative permeabilities of liquid and gas phases, respectively

$$k_{rk} = \frac{K_k}{K} \quad [8]$$

In this work, we assume the relative permeabilities of individual phases are related to the cube of phase saturations, i.e.,[10]

$$k_{rk} = s_k^3 \quad [9]$$

where s_k is the saturation of phase k.

Phase saturations, s_k are defined as the fraction of the open pore volume occupied by that individual phase; hence the liquid saturation, s is defined as

$$s = \frac{V_l}{V} \quad [10]$$

Wang and Cheng[28] define the mixture mass fraction as

$$\rho mf^i = \rho_g mf_g^i(1-s) + \rho_l mf_l^i s \quad [11]$$

which leads to definition of liquid saturation from the total water concentration, C^{H_2O} via

$$s = \frac{\rho mf^{H_2O} - \rho_g mf_g^{H_2O}}{\rho_l mf_l^{H_2O} - \rho_g mf_g^{H_2O}} = \frac{C^{H_2O} - C_{sat}^{H_2O}}{C_l^{H_2O} - C_{sat}^{H_2O}} \quad \text{where } C_l^{H_2O} = \frac{\rho_l}{M^{H_2O}} \quad [12]$$

Because oxygen and nitrogen are assumed to be insoluble in liquid water due to very low solubility,[32] liquid phase only includes water, i.e., $mf_l^{H_2O} = 1$.

Upon accounting for anisotropy of the diffusion media, the effective gas diffusion coefficient, $\mathbf{D}_g$ becomes a second-rank tensor, as the effective diffusivities in the in-plane and through-plane direction are significantly different due to the fiber orientation of the GDL, as seen in Fig. 2. The treatment of anisotropic diffusivity in the numerical model is explained in Appendix . Nam and Kaviany[21] have investigated the effective gas diffusion coefficients in the GDL, using a pore network model. Their predictions agreed well with the previous correlations of Tomadakis and Sotirchos[33] on fibrous porous media

$$\mathbf{D}_g^{i,\text{eff}} = f(\varepsilon)D_g^i$$

$$\text{where } f(\varepsilon) = \varepsilon\left(\frac{\varepsilon - \varepsilon_p}{1-\varepsilon_p}\right)^\alpha \quad \alpha = \begin{matrix} 0.521 & \text{in-plane direction} \\ 0.785 & \text{through-plane direction} \end{matrix} \quad [13]$$

This effective diffusion model predicts that in-plane diffusion coefficient is larger than the through-plane counterpart. The structured

orientation of fibers in the in-plane direction causes a less tortuous path for gas diffusion than that in the through-plane direction, in which fibers are more randomly oriented resulting in more tortuous gas diffusion path.

The last term on the right-hand side of the species conservation equation (Eq. 5) represents the capillary transport in the porous media. The theory of capillary transport in hydrophobic PEFC GDLs has been explained by Pasaogullari and Wang.[15] The capillary flux, $\mathbf{j}_l$, is defined as[28]

$$\mathbf{j}_l = \frac{\lambda_l \lambda_g}{\nu} K[\nabla p_c + (\rho_l - \rho_g)\mathbf{g}] \quad [14]$$

where p_c is the capillary pressure and is given by[28]

$$p_c = \sigma \cos(\theta_c)\left(\frac{\varepsilon}{K}\right)^{1/2} J(s) \quad [15]$$

where, $J(s)$ is the Leverett function and, for both hydrophobic and hydrophilic GDL, is given as[15]

$$J(s) = \begin{cases} 1.417(1-s) - 2.120(1-s)^2 + 1.263(1-s)^3 & \text{if } \theta_c < 90^\circ \\ 1.417s - 2.120s^2 + 1.263s^3 & \text{if } \theta_c > 90^\circ \end{cases} \quad [16]$$

The above Leverett function was proposed by Udell[34] for packed beds, and its applicability to PEFC GDL requires experimental verification, which is still absent in the literature.

Because the permeability of the GDL differs by up to an order of magnitude in the in-plane and through-plane directions, the capillary liquid water flow is no longer isotropic; hence we also account for the anisotropy in liquid water flow via

$$j_x = \frac{\lambda_l \lambda_g}{\nu} K_{xx}\left[\frac{\partial p_c}{\partial x} + (\rho_l - \rho_g) g_x\right]$$

$$j_y = \frac{\lambda_l \lambda_g}{\nu} K_{yy}\left[\frac{\partial p_c}{\partial y} + (\rho_l - \rho_g) g_y\right] \quad [17]$$

where K_{xx} and K_{yy} denote the permeabilities in the through-plane and in-plane directions, respectively. Through-plane permeability of the PEFC GDLs has been characterized by Williams et al.,[35] and the permeability of Toray carbon paper (TGPH-090) has been found to be 8.69×10^{-12} m^2. On the other hand, in-plane permeability of carbon-paper GDLs has been reported to be in the range of $1.9 - 4.7 \times 10^{-12}$ m^2 by Bluemle et al.[36]

When applied to water, the species equation, Eq. 5, implies that the water transport within a two-phase zone is due to gas phase diffusion (i.e., the first term on the right-hand side) and capillary action (i.e., second term on the right-hand side), in addition to advection. The gas phase diffusion driven by the gradient in saturation concentration vanishes in an isothermal two-phase zone as saturation concentration is only a function of temperature, but can be significant in a nonisothermal, two-phase zone. In the latter case, the gas phase diffusion of water aids in the capillary transport in the through-plane direction (i.e., from catalyst layer toward gas channel) because both fluxes are directed outside of the GDL. However, the two are opposed to each other in the in-plane direction where the gas phase diffusive flux of water is pointed from the channel region (hotter) toward the land region (cooler), while the capillary flux of liquid water is from the land (higher liquid saturation) to channel regions.

Energy conservation.— The energy conservation equation in M^2 model for the GDL is[28]

$$\frac{\partial}{\partial t}\{[(1-\varepsilon)(\rho c_p)_s + \varepsilon \rho c_p]T\} + \nabla \cdot (\gamma_h \rho c_p \mathbf{u} T) = \nabla \cdot (\mathbf{k}^{\text{eff}} \nabla T) + S_{T,PC} \quad [18]$$

This equation describes the conductive and convective heat-transfer in PEFCs and a heat source/sink due to condensation and evaporation. Because the pore size of the GDL is relatively small (~ 10 μm), and advection within the GDL is negligible, the solid and fluid temperatures are taken to be equal. The terms on the left-hand side of Eq. 18 are the transient and advective terms, respectively. In the transient term, $(1-\varepsilon)(\rho c_p)_s + \varepsilon \rho c_p$ represents the total heat capacitance of the porous medium, consisting of solid matrix and two-phase mixture occupying the open pores. Again, because the liquid and gas phases have different flow-fields, the advective heat-transfer is corrected via[28]

$$\gamma_h = \frac{\rho(\lambda_l c_{p,l} + \lambda_g c_{p,g})}{s\rho_l c_{p,l} + (1-s)\rho_g c_{p,g}} \quad [19]$$

The last term on right-hand side of Eq. 18 describes the heat release or adsorption due to phase change (i.e., condensation or evaporation) and is given by

$$S_{T,PC} = h_{fg} \dot{m}_{fg} \quad [20]$$

where h_{fg} is the latent heat of condensation/evaporation and $\dot{m}_{fg}$ the mass rate of phase change that can be readily calculated from the continuity equation of liquid phase, which consists of only water

$$\dot{m}_{fg} = \nabla \cdot (\rho_l u_l) \quad [21]$$

The liquid phase velocity is calculated using

$$\rho_l \mathbf{u}_l = \mathbf{j}_l + \lambda_l \rho \mathbf{u} \quad [22]$$

Substituting Eq. 21 into Eq. 20 yields

$$\dot{m}_{fg} = \nabla \cdot (j_l + \lambda_l \rho u) \quad [23]$$

Thermal conductivity of the GDL also exhibits anisotropy, and it is found that the in-plane GDL conductivity may be larger by up to 14 times than that of in the through-plane direction.[37] Therefore, the anisotropy of the GDL solid matrix is also accounted for heat conduction in the GDL via effective conductivity tensor, k^{eff} as explained in the Appendix. Accordingly, conduction heat flux in GDL becomes

$$\mathbf{j}_{\text{cond}} = -\mathbf{k}^{\text{eff}} \cdot \nabla T = j_x \mathbf{i} + j_y \mathbf{j}$$

$$j_x = -[(1-\varepsilon_{GDL})k_{GDL}^{\text{through-plane}} + \varepsilon_{GDL} k_f]\frac{\partial T}{\partial x}$$

$$j_y = -[(1-\varepsilon_{GDL})k_{GDL}^{\text{in-plane}} + \varepsilon_{GDL} k_f]\frac{\partial T}{\partial y} \quad [24]$$

Electronic charge conservation.— Electronic charge conservation equation is

$$\nabla \cdot (\boldsymbol{\sigma}^{\text{eff}} \nabla \phi_s) = 0 \quad [25]$$

where the conductivity, $\boldsymbol{\sigma}^{\text{eff}}$ is a second rank tensor accounting for the anisotropy in the GDL electronic conductivity. The boundary conditions for this equation are specified at the GDL-current collector interface as the prescribed cell voltage and at the catalyst layer-GDL interface as the current density (i.e., electronic current).

Consequently, the model accounts for the complete anisotropy of GDL, including anisotropy in thermal conductivity, electronic conductivity, species diffusion and capillary transport of liquid water.

Boundary conditions.— The water production and heat generation rates are linearly related to current density distribution. However, our modeling domain only includes the cathode GDL, therefore the following assumptions must be made in order to predict the current density.

1. Water content of the membrane and catalyst layers is only a function of cathode side water concentration and temperature. This assumption will only hold true if the anode side is also fully saturated and the net water transport across the membrane is small, resulting in small water content gradients across the membrane. In addition, net water transport coefficient, α is also assumed to be zero, which is a reasonable assumption for thinner membranes

($\sim$25 μm). Note that zero net water transport coefficient is a representative value for the present study, although significant variation of net water transport coefficient, including negative, zero, and positive values corresponding to the PEFC operating conditions, has been reported in the literature.[38]

2. Concentration overpotential of the anode hydrogen oxidation reaction (HOR) is negligible.

3. Bipolar plates are perfectly electronically conductive, i.e., negligible ohmic losses across the bipolar plates.

4. The cathode catalyst layer is a thin interface between the GDL and the membrane.

Following these assumptions, we calculate the current density distribution as follows.

The cell potential is equal to

$$V_{\text{cell}} = U_{\text{oc}}(T) - \eta_{\text{a}} - \eta_{\text{c}} - IR_{\Omega} \quad [26]$$

where R_{Ω} is the ionic resistance of membrane and catalyst layers

$$R_{\Omega} = \frac{\delta_{\text{mem}}}{\kappa_{\text{e}}} + 2\frac{\delta_{\text{CL}}}{\kappa_{\text{e}}\varepsilon_{\text{mc}}^{1.5}}\frac{I_{\text{CL}}^{\text{ave}}}{I} \quad [27]$$

The anode activation polarization is described as follows, using a linear kinetics approximation due to facile anode electrochemical kinetics in PEFCs

$$\eta_{\text{a}} = \frac{IRT}{(\alpha_{\text{a}} + \alpha_{\text{c}})Fai_{\text{o}}^{\text{ref,a}}} \quad [28]$$

The cathode activation polarization is described via Tafel kinetics due to higher overpotentials

$$\eta_{\text{c}} = \frac{RT}{\alpha_{\text{c}}F}\ln\left(\frac{C_{\text{O}_2}^{\text{ref}}}{C_{\text{O}_2}}\frac{I}{ai_{\text{o}}^{\text{ref,c}}}\right) \quad [29]$$

Combining Eq. 26-29

$$V_{\text{cell}} = U_{\text{oc}}(T) - \frac{IRT}{(\alpha_{\text{a}} + \alpha_{\text{c}})Fai_{\text{o}}^{\text{ref,a}}} - \frac{RT}{\alpha_{\text{c}}F}\ln\left(\frac{C_{\text{O}_2}^{\text{ref}}}{C_{\text{O}_2}}\frac{I}{ai_{\text{o}}^{\text{ref,c}}}\right) - IR_{\Omega} \quad [30]$$

which is a nonlinear equation with only one unknown, current density, I for a given cell voltage. This nonlinear equation is solved at the GDL-CL interface using a bisection method, with an accuracy of up to 10^{-8} A/cm^2.

We note that the prediction of current density is not meant to be thoroughly accurate because it involves certain assumptions; hence it is only used as an input to the model. For accurate prediction of current density, modeling domain must be extended to include the anode and the membrane, which is outside the scope of this work.

Given the current distribution, the boundary conditions are as follows.

Catalyst-layer-GDL interface (left boundary in Fig. 3a, line AB).— The total mass flux due to consumption/production of all species is given by

$$\mathbf{j}_m\mathbf{n}_{\text{GDL-CL}} = \frac{I}{2F}\left[(1 + 2\alpha)M^{\text{H}_2\text{O}} - \frac{1}{2}M^{\text{O}_2}\right] \quad [31]$$

The water flux due to water production and net water transport from anode can be expressed as

$$\mathbf{j}_{\text{H}_2\text{O}}\mathbf{n}_{\text{GDL-CL}} = \frac{I}{2F}(1 + 2\alpha) \quad [32]$$

where α is the net water transport coefficient across the membrane, and in this work it is assumed to be zero, because the membrane is assumed to be very thin (25.4 μm Nafion 111).

Because the anode and the electrolyte are not included in the modeling domain, we also must assume the distribution of heat generation rate. It is assumed that all the heat generation associated with cathode ORR and half of the joule heating due to ohmic losses is transported through cathode. Note that the assumption of the fraction of the total heat transported through the GDL is rather a mathematical input into the current cathode-only GDL model while its justification might be physically lean similar to earlier cathode-only GDL model reported in Ref. 21. The resulting heat flux at the GDL-catalyst layer interface then becomes

$$q''_{\text{GDL-CL}} = I\left(\eta_{\text{c}} + T\frac{dU_{\text{oc}}}{dT} + \frac{1}{2}R_{\Omega}\right) \quad [33]$$

The latent heat effects due to condensation/evaporation in the GDL is not included in this term, because it is calculated via continuity of liquid water flow as explained in Eq. 23, and included as heat source/sink in the energy conservation equation. Here it is assumed that water enters the GDL in the same phase as in GDL.

Current collector–GDL interface (top-right boundary in Fig. 3a, line CD).— The current collectors, typically graphite or metal, has large thermal conductivities; therefore, the temperature at this interface is taken to be equal to the given cell temperature. Note that this also includes an inherent assumption of zero contact resistance between the current collector and GDL

$$T_{\text{GDL-CC}} = T_{\text{cell}} \quad [34]$$

As the current collector is impermeable, a zero-flux boundary condition for species and no-slip velocity boundary condition are prescribed at the current collector-GDL interface.

Gas channel–GDL interface (bottom-right boundary in Fig. 3a, DE).— The gas pressure is taken to be equal to the operating pressure of the PEFC (i.e., 1 atm), and the capillary pressure at this interface is equal to zero. A convective heat-transfer boundary is utilized and the convective heat-transfer coefficient is calculated from correlations for the laminar flow in square cross-section ducts[39] as 25 W/m^2 K and the free-stream temperature is taken equal to the operating temperature of the cell (i.e., 80°C). The water concentration is taken to be equal to the saturation water concentration at the cell temperature, typical of an inlet section of fully humidified cathode.

At the top and bottom boundaries (lines AE and BC), symmetry boundary conditions are applied.

Numerical implementation.— The resulting set of equations is discretized using a finite-volume method[40] and solved within the commercially available CFD software, Fluent, by customizing via user defined functions (UDF).[41] Fluent provides the flexibility of solving a generic advection-convection equation

$$\frac{\partial(R\phi)}{\partial t} + \nabla\cdot(J\phi) = \nabla\cdot(\mathbf{\Gamma}\nabla\phi) + S \quad [35]$$

The variables R, $\mathbf{J}$, $\mathbf{\Gamma}$, and S are customized via user-defined functions. The species conservation equations and energy equations are implemented using this generic scalar equation template.

The software utilizes the well-known SIMPLE algorithm for pressure-velocity coupling, and an algebraic multigrid (AMG) solver to efficiently solve the set of discretized linear equations. For details of the SIMPLE algorithm, the reader is referred to Ref. 40

Grid independence study.— A grid independence study is carried out to determine the required grid resolution. The results are shown in Fig. 4, and as seen 2400 computational cells (40 computational cells in the through-plane direction, 60 computational cells in the in-plane direction) are found to be adequate and computational time required for the 2-D nonisothermal two-phase results shown in this work is around 10 min on a single PC (2 GB RAM, 1.66 GHz).

Results and Discussion

To investigate the effects of GDL anisotropy, two different GDLs were simulated at the same operating conditions, at 353.15 K cell temperature and 1 atm operating pressure. The two-dimensional domain corresponds to inlet region of a PEFC operated with fully humidified air at the described conditions. The first GDL is isotropic with uniform transport properties in all directions. The properties are

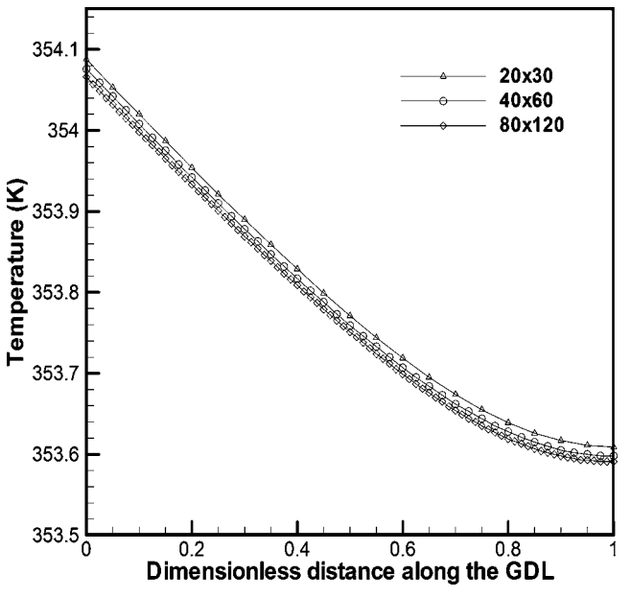

Figure 4. Temperature profile across the GDL under the gas channel from the grid independence study.

taken from Toray TGPH carbon paper[37] and the values for the through plane direction is used for all directions for the isotropic GDL. The second GDL is anisotropic and the principal axes of the porous media (i.e., GDL) coincide with the coordinate axes (i.e., orthotropic). The through-plane and in-plane values of the thermal and electronic conductivity for this GDL are again taken from Toray TGPH carbon paper.[37] The transport properties are listed in Table I.

Figure 5 shows the cathode polarization curve for both isotropic and anisotropic GDL. Because the boundary condition on the channel side is taken to be at the inlet, oxygen concentration is high; therefore polarization curve does not show any mass transfer limitation effects, even at higher current densities. The overall performance at this location is limited by the ionic conductivity of membrane and catalyst layers. Both GDLs show very similar performance at relatively low current densities; however, the performances start to differ at high current densities due to limited electronic conductivity of isotropic GDL in the in-plane direction. As seen in Fig. 6, due to lower electronic conductivity in the in-plane direction, electron transport in the in-plane direction requires higher electronic phase potential gradient, resulting in higher electronic potential at the regions underneath the gas channel for isotropic GDL. As the current flows through the current collector ribs, the distance for current flow is longer for those regions underneath the channel, and in turn requires higher potential difference. In contrast, the elec-

Table I. Physical parameters and properties.

Parameters/properties	Value
Modeling domain dimensions and GDL properties	
Cathode GDL thickness	300 μm
Half channel width	500 μm
Half current collector rib width	250 μm
GDL porosity, ε	0.7
Through-plane GDL permeability	8.69×10^{-12} m^2[35]
In-plane GDL permeability	3.00×10^{-12} m^2[36]
Through-plane thermal conductivity	1.7 W/m K[37]
In-plane thermal conductivity	21 W/m K[37]
Through-plane electronic conductivity	1250 S/m[37]
In-plane electronic conductivity	17857 S/m[37]
GDL contact angle, θ_c	110°
Fluid properties	
Thermal conductivity of liquid water[a]	$(0.621529 + 6.05 \times 10^{-4}\ \theta)$W/m K
Viscosity of liquid water[a]	$(7.0968 - 0.0444\theta) \times 10^{-4}$ Pa s
Density of liquid water[a]	$(1021.516 - 0.622\theta)$kg/m^3
Gas mixture viscosity[44]	$\mu_g = \sum_{i=1}^{N} \frac{x_i \mu_i^g}{\sum_{k=1}^{N} d_k[8(1+MW_i/MW_k)]^{-0.5}[1+\sqrt{\mu_i^g/\mu_k^g}(MW_k/MW_i)^{1/4}]^2}$
Water vapor viscosity[a]	$(0.8918 + 0.003344\theta) \times 10^{-5}$ Pa s
Nitrogen viscosity[a]	$(1.6824 + 0.004294\theta) \times 10^{-5}$ Pa s
Oxygen viscosity[a]	$(1.9267 + 0.005159\theta) \times 10^{-5}$ Pa s
Gas density	$\rho_g = \sum_{i=1}^{N} C_i^g MW_i$ where $C_{N_2}^g = p_g/RT - C_{H_2O}^g - C_{O_2}^g$
Gas mixture thermal conductivity[44]	$k_g = \sum_{i=1}^{N} x_i k_i^g \Big/ \sum_{k=1}^{N} d_k[8(1 + MW_i/MW_k)]^{-0.5}[1 + \sqrt{\mu_i^g/\mu_k^g}(MW_k/MW_i)^{1/4}]^2$
Thermal conductivity of water vapor[a]	$(0.0152084 + 9.757 \times 10^{-5}\theta)$W/m K
Thermal conductivity of oxygen[a]	$(0.024508 + 8.021 \times 10^{-5}\theta)$W/m K
Thermal conductivity of nitrogen[a]	$(0.024255 + 6.313 \times 10^{-5}\theta)$W/m K
Binary gas diffusion coefficient[45]	$D_{AB} = \frac{1}{p} a\left(T/\sqrt{T_{cA}T_{cB}}\right)^b (p_{cA}p_{cB})^{1/3}(T_{cA}T_{cB})^{5/12}\left(\frac{1}{M_A} + 1/M_B\right)^{1/2}$
Surface tension[a]	$(7.731 - 0.0183\theta)10^{-2}$ N/m
Water saturation pressure	$10^{2.826317+0.02953\theta-9.1837\times10^{-5}\theta^2+1.4454\cdot10^{-7}\theta^3}$ Pa
$\theta = \frac{(T-273.15\ \mathrm{K})}{\mathrm{K}}$ where T is local temperature in K	

[a] Data is obtained by curve-fitting NIST Chemistry Webbook[43] data in relevant temperature range.

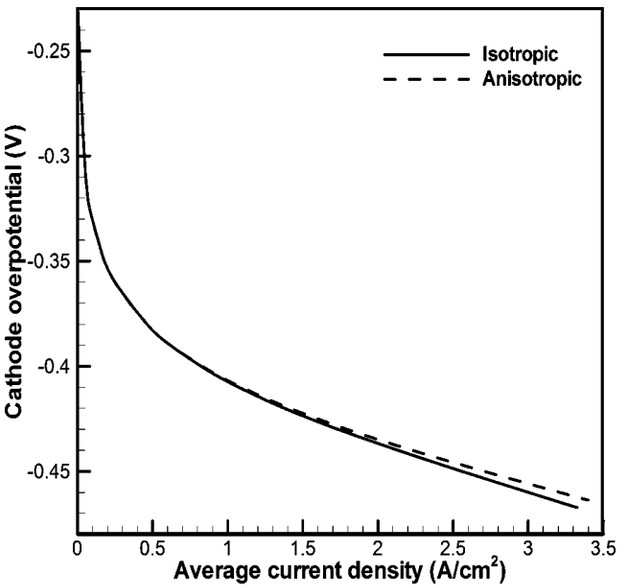

Figure 5. Cathode polarization curves for isotropic and anisotropic GDLs.

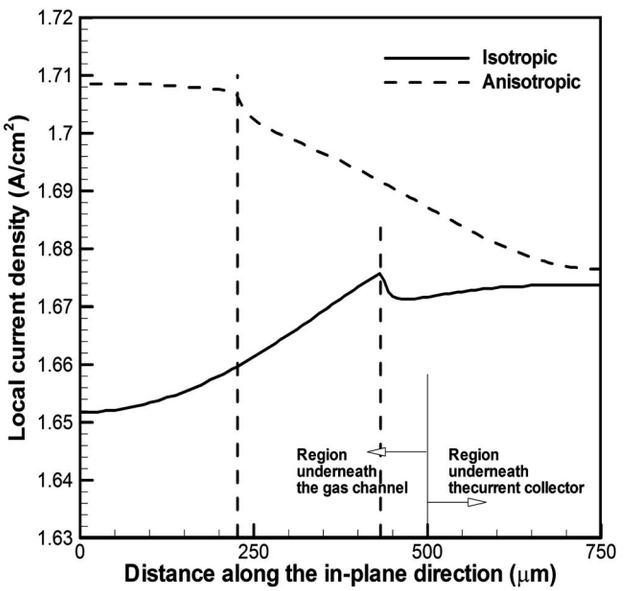

Figure 7. Current density distributions at the CL-GDL interface at 0.4 V cell voltage for both the isotropic and anisotropic GDLs.

tronic potential profile for an anisotropic GDL shows almost a one-dimensional behavior with very little variation in the in-plane direction due to large conductivity. Note that Toray TGPH series carbon paper has almost 15 times higher electronic conductivity in the in-plane direction than that in the through-plane direction.

The effect of GDL anisotropy is clearly pronounced in the current density distributions at the catalyst layer-GDL interface, as shown in Fig. 7. In the anisotropic GDL, the current density mainly follows the oxygen concentration at the catalyst-layer-GDL interface, as shown in Fig. 8, indicating that the reaction is mainly limited by mass transfer effects. On the other hand, isotropic GDL shows an interesting profile with lower current density values under the gas channel even though the oxygen concentration is higher in those areas, and a higher current density in regions closer to the current collector. This profile indicates that for the isotropic GDL, both oxygen concentration and electronic potential affect the current distribution, each dominating in different parts of the active catalyst layer. Discontinuities in the current density profiles are related to liquid water distribution and resulting effective oxygen diffusivity, and are discussed later in detail with liquid saturation distributions.

Figure 9 shows the temperature contours in the GDL for two different cell voltages, 0.6 and 0.4 V, respectively. Perhaps, the most profound effect of the GDL anisotropy is seen in the temperature profiles. The isotropic GDL has equal conductivities in both in-plane and through plane directions, i.e., 1.7 W/m K, which is equal to the through-plane value.[37] It is seen here that a maximum temperature difference of up to 2°C in 0.6 V and 5°C in 0.4 V is observed for the isotropic GDL. Note that the heat generation rate at 0.4 V is

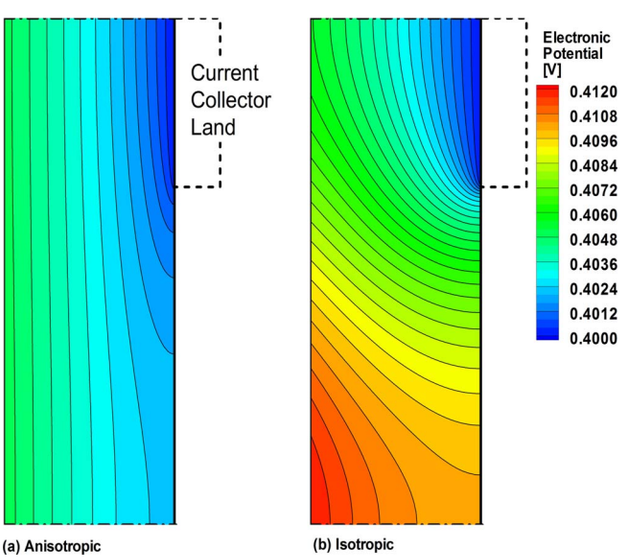

Figure 6. (Color online) Electronic phase potential distributions at 0.4 V cell voltage for both the isotropic and anisotropic GDLs. (a) Anisotropic GDL and (b) isotropic GDL.

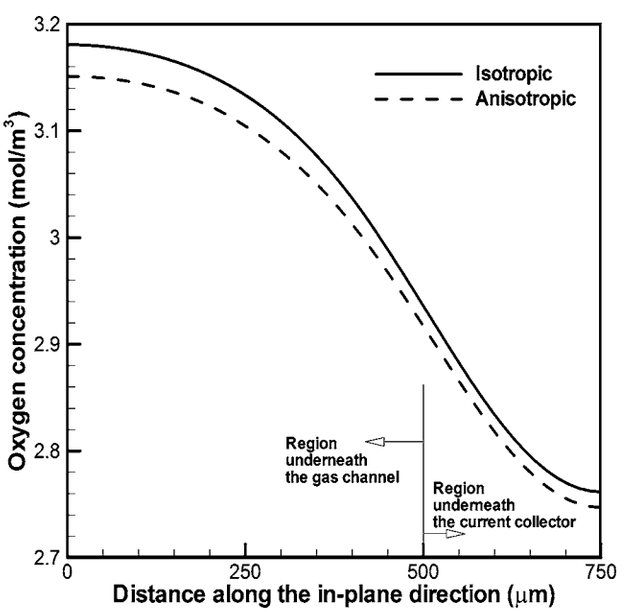

Figure 8. Oxygen concentration distribution at the CL-GDL interface at 0.4 V cell voltage for both the isotropic and anisotropic GDLs.

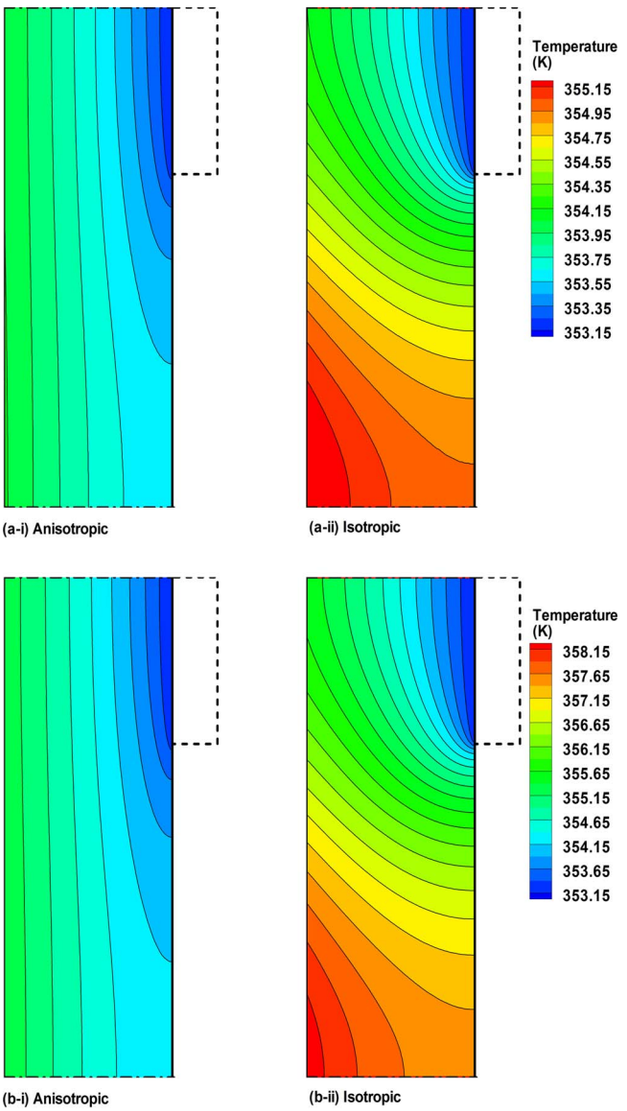

Figure 9. (Color online) Contours of temperature distribution for both the isotropic and anisotropic GDLs. (a-i) Anisotropic GDL at 0.6 V, (a-ii) isotropic GDL at 0.6 V, (b-i) anisotropic GDL at 0.4 V, and (b-ii) isotropic GDL at 0.4 V.

roughly 2.5 times of that at 0.6 V. Similar to electronic phase potential, temperature profile also shows a maximum underneath the gas channel. Because most of the heat generated (up to 99% as predicted by the results here) is transported through current collectors, main conductive heat-transfer path is from under the channel towards current collector, where typically coolant channels are located. This requires that the heat generated under the channel has to travel in the in-plane direction; therefore in-plane conductivity becomes the dominating parameter governing the temperature distribution. In the anisotropic simulation with in-plane thermal conductivity of 21 W/m K and through-plane conductivity of 1.7 W/m K,[37] the temperature profile becomes almost one-dimensional, varying mostly in the through-plane direction. However, in the isotropic case with 1.7 W/m K in-plane thermal conductivity, a highly nonuniform temperature distribution in the GDL is observed. The temperature is higher near the catalyst layer, because the heat flow is mainly by conduction. Furthermore, there is also a strong temperature gradient in the GDL from the region underneath the channel to the region underneath the land. This profile again indicates that the heat-transfer from the GDL is mainly through the current collector land, that is, the land acts as a heat sink for the GDL. In anisotropic GDL, it is seen that the temperature distribution in the GDL is more uniform and maximum temperature is lower than the isotropic case. Although the thermal conductivity in the through-plane direction has the same value for both isotropic and anisotropic cases, the heat-transfer in the in-plane direction is much more effective with anisotropic GDLs due to higher conductivity; therefore, temperature differences are smaller, resulting in a more uniform temperature profile. The choice of higher thermal conductivity, e.g., equal to the in-plane value of 21 W/m K, in the isotropic case will result in an unreasonably low value of the maximum temperature difference in the GDL, namely only a fraction of 1°K. In either case, the isotropic GDL simulation not only exhibits anomalous temperature distribution but also either overpredicts or underpredicts the maximum temperature difference in the GDL depending on the chosen thermal conductivity value as compared to the anisotropic simulation. This observation further underscores the importance of GDL anisotropy in the underlying heat and water distributions as explained further in the subsequent subsections.

When the liquid saturation distributions in Fig. 10 were investigated, it was not surprising to see that most significant effects of GDL anisotropy were seen in the distribution of the liquid water. Liquid water distribution is a result of a combined effect of temperature distribution, oxygen distribution, and electronic phase potential distribution, as they govern the water production rate through the current density. Temperature distribution becomes especially important because the saturation concentration, which governs condensation of water, is a direct function of temperature as shown in Fig. 1. As seen in Fig. 10, the anisotropic GDL predicts a larger portion of GDL being flooded with water compared to the isotropic GDL, because the overall lower temperature of the anisotropic GDL causes total water concentration to reach saturation concentration in a larger portion of the GDL. In the isotropic GDL, liquid water is mostly seen under the current collectors due to lower temperatures in this region, however in the anisotropic GDL, liquid water is also seen under the gas channels. However, note that, the simulation results presented here represent near-the-inlet region of a PEFC with fully humidified cathode inlet. In the actual PEFC system, the channel water concentration would increase along the channel due to water production; therefore, the entire GDL cross section may become flooded, as is apparent from the anisotropic simulation while the isotropic simulation might still exhibit partial flooding. A full-cell PEFC model with anisotropic heat and water transport through the GDL is described in a separate publication, which provides a better understanding of the along-the-channel water distributions and the corresponding flooding scenario.

It is also seen that the maximum liquid saturation, which occurs underneath the current collectors in both cases, is higher in anisotropic GDLs. This is due to the fact that, in the anisotropic GDL, liquid water transport in the in-plane direction is less effective due to lower permeability. Because the in-plane permeability is lower, it requires a larger pressure gradient to drive the same liquid water flow, thereby requiring higher liquid saturation differential. Also note that the distance between the maximum liquid saturation point and evaporation front is much longer in the anisotropic GDL, which contributes to the requirement of higher liquid pressure differential.

Unlike in an isothermal two-phase zone, there is water transport in vapor diffusion mode in a nonisothermal two-phase zone due to variation in saturation vapor concentration with temperature. This mode of vapor diffusion is from the high temperature regions to low temperature regions, as saturation concentration of water vapor increases with temperature as shown in Fig. 1. In the isotropic GDL, there is temperature variation in both in-plane and through-plane directions, which results in water transport from the higher temperature region (under the middle of gas channel) to the lower temperature region (under the current collector). The water vapor then condenses underneath the current collector due to lower temperature, releasing heat. This mode of heat-transfer is referred to as “heat pipe

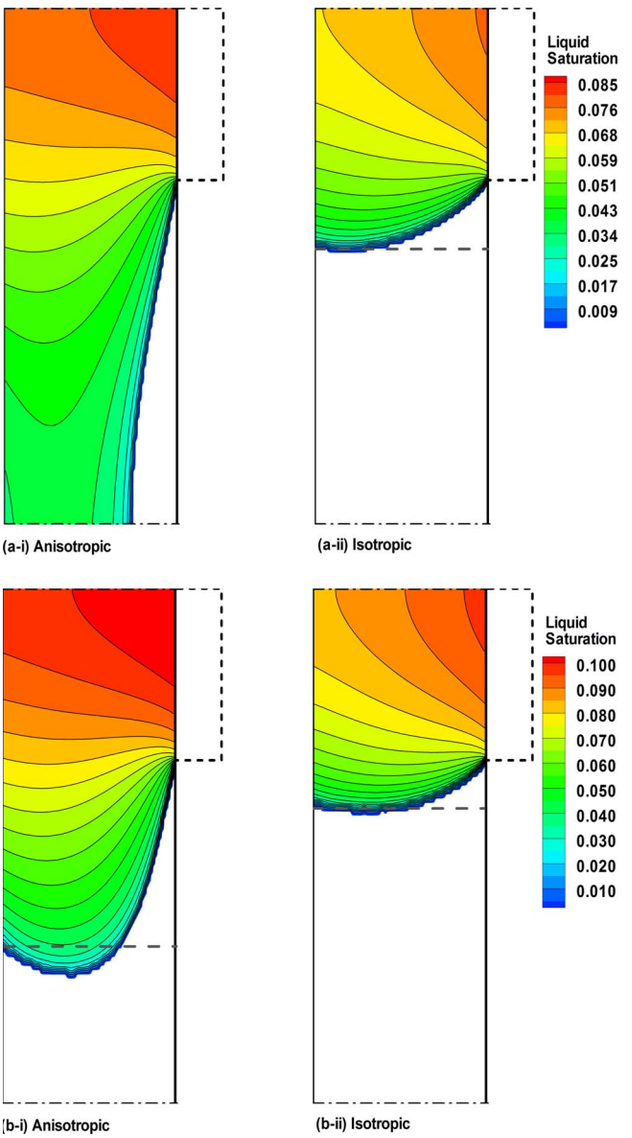

Figure 10. (Color online) Contours of liquid water saturation distribution for both the isotropic and anisotropic GDLs. (a-i) Anisotropic GDL at 0.6 V, (a-ii) isotropic GDL at 0.6 V, (b-i) anisotropic GDL at 0.4 V, and (b-ii) isotropic GDL at 0.4 V.

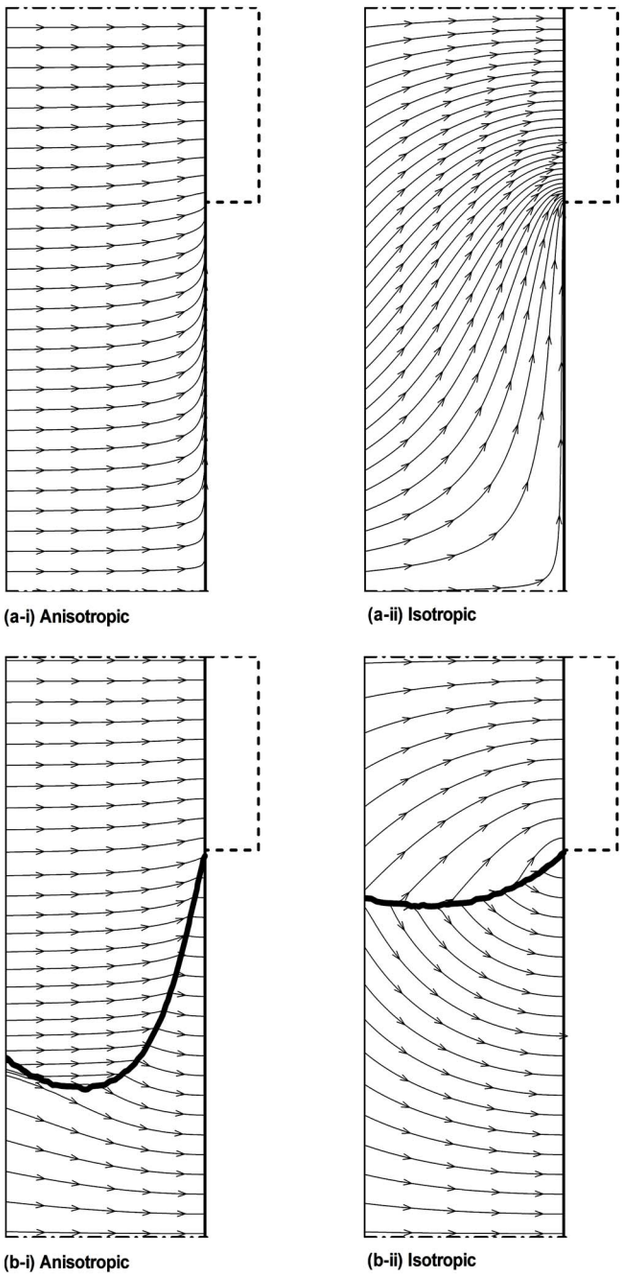

Figure 11. Conductive heat flux and vapor diffusion flux pathlines at 0.4 V cell voltage for both the isotropic and anisotropic GDLs. (a-i) Conductive heat flux pathlines for the anisotropic GDL, (a-ii) conductive heat flux pathlines for the isotropic GDL, (b-i) vapor diffusion flux pathlines for the anisotropic GDL, and (b-ii) vapor diffusion flux pathlines for the isotropic GDL. Thick gray lines represent the predicted condensation front.

effect" by Wang and Wang[31] and found to be in comparable order with heat conduction. In our model predictions, we also see similar effects in isotropic GDL; however in the anisotropic model this effect vanishes because the temperature variation in the in-plane direction is minimal, minimizing any water vapor diffusion due to saturation concentration gradients in the in-plane direction.

To investigate the effect of anisotropy in the overall transport of heat and water vapor diffusion, conductive heat-transfer and water vapor diffusion pathlines are plotted in Fig. 11 for both anisotropic and isotropic GDLs at 0.4 V. The conductive heat-transfer pathlines are calculated from the conductive heat flux vectors, which are calculated via

$$\mathbf{j}^{\text{Heat}} = -\sum k_i \frac{\partial T}{\partial x_i}\mathbf{i}_i \qquad [36]$$

where k_i is the effective conductivity in direction i. It is seen from Fig. 11a that the conductive heat flux follows different paths for isotropic and anisotropic GDLs. In the isotropic GDL, a diagonal path from the region under the channel closer to catalyst layer toward the current collector is observed. As can be deduced from the temperature contours in Fig. 9b, in the anisotropic GDL, the heat-transfer is almost one-dimensional in the through-plane direction, and most of the lateral (in the in-plane direction) heat-transfer occurs in regions very close to channel-GDL interface.

Figure 11b shows the water vapor diffusion pathlines, which is calculated similar to heat conduction pathlines

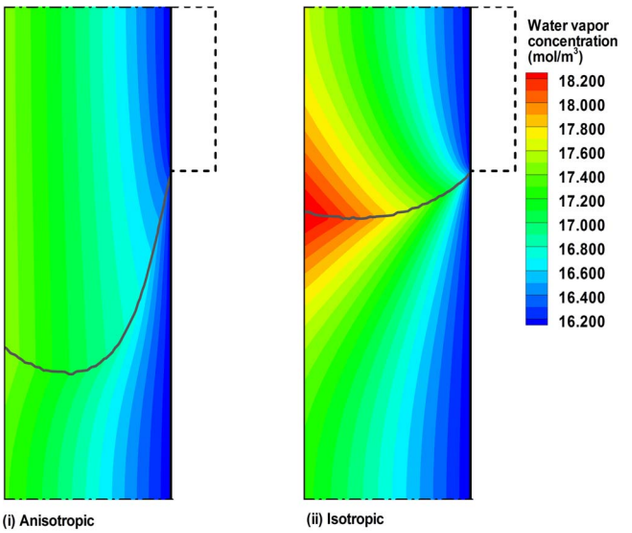

Figure 12. (Color online) Water vapor concentration contours at 0.4 V cell voltage for both the isotropic and anisotropic GDLs. (i) Anisotropic GDL and (ii) isotropic GDL. Thick gray lines represent the predicted condensation front.

$$\mathbf{j}^{\mathrm{H_2O}} = -\sum D_i^{\mathrm{H_2O,eff}} \frac{\partial C_{\mathrm{H_2O}}^{\mathrm{g}}}{\partial x_i} \mathbf{i}_i \qquad [37]$$

It is seen that the principal direction for water vapor diffusion is the through-plane direction in both anisotropic and isotropic GDLs. However, it is also seen that water vapor diffusion follows the temperature contour shown in Fig. 9b in the two-phase region as water vapor concentration is equivalent to saturation concentration. Therefore, water vapor diffusion in two-phase region can be written as

$$\mathbf{j}_{\mathrm{H_2O}}^{\mathrm{eff}} = -\sum D_i^{\mathrm{H_2O,eff}} \frac{\partial C_{\mathrm{H_2O}}^{\mathrm{sat}}}{\partial x_i} \mathbf{i}_i = -\sum D_i^{\mathrm{H_2O,eff}} \frac{dC_{\mathrm{H_2O}}^{\mathrm{sat}}}{dT} \frac{\partial T}{\partial x_i} \mathbf{i}_i$$

$$= \frac{dC_{\mathrm{H_2O}}^{\mathrm{sat}}}{dT} \sum \frac{D_i^{\mathrm{H_2O,eff}}}{k_i} j_i^{\mathrm{Heat}} \qquad [38]$$

and it becomes a function of temperature gradient. Therefore, vapor diffusion follows similar pathlines to conductive heat-transfer flux in the two-phase region. Another interesting feature shown in Fig. 11b is that the vapor diffusion changes direction at the condensation front, both visible at isotropic and anisotropic GDLs. As seen in Fig. 12, vapor concentration has a peak at the condensation front and vapor diffusion is from condensation front toward the current collector in the two-phase region and it is from condensation front to GDL-channel interface in the single-phase region.

Figure 13 and 14 show the liquid and gas phase flow-fields, respectively. As seen in Fig. 13, liquid pressure has a maximum colocated with the highest liquid saturation as shown in Fig. 10, and liquid water flow is from higher liquid saturation to lower liquid saturation. Note that there is no liquid water flow in single-phase regions. In contrast, gas phase pressure is higher at the GDL-channel interface and gas flow is from high gas pressure locations to low gas pressure locations. It is also seen that gas velocity is significantly higher in two-phase regions than it is in single-phase regions. The reason for this is that the velocities plotted here are mass averaged: In single-phase zone the gas velocity can be approximated as

$$\rho_{\mathrm{gas}} \mathbf{u}_{\mathrm{gas}} = \mathbf{j}_{\mathrm{H_2O}} M_{\mathrm{H_2O}} + \mathbf{j}_{\mathrm{O_2}} M_{\mathrm{O_2}} = \frac{I}{2F}(1 + 2\alpha) M_{\mathrm{H_2O}} - \frac{I}{4F} M_{\mathrm{O_2}} \qquad [39]$$

Assuming α is zero

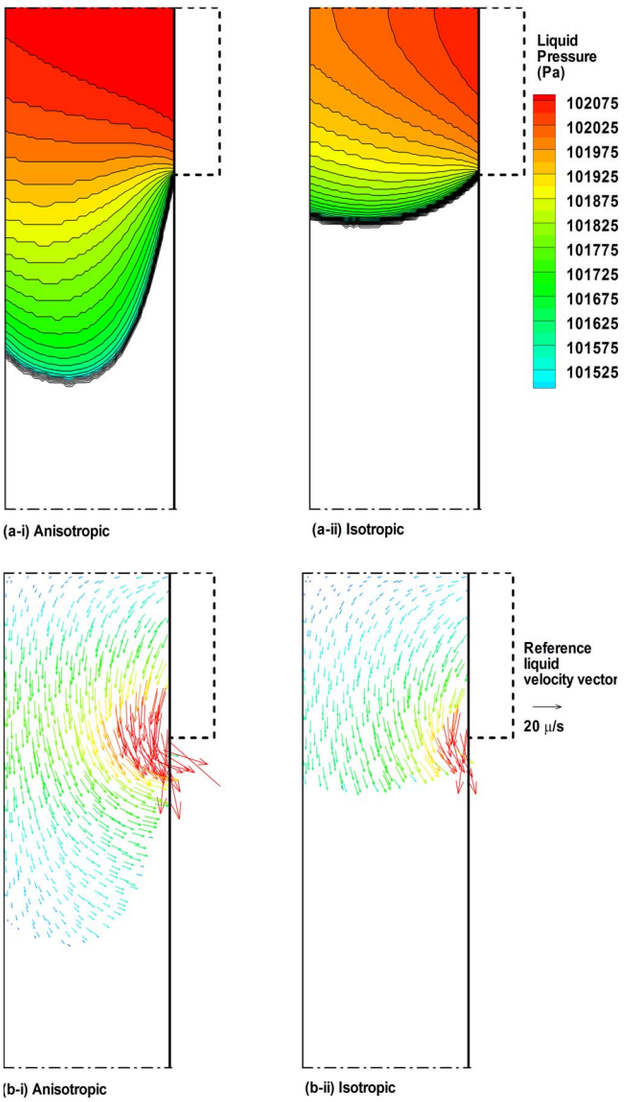

Figure 13. (Color online) Pressure contours and velocity vectors at 0.4 V cell voltage pertaining to the liquid flow-field for both the isotropic and anisotropic GDLs. (a-i) Liquid pressure contour for the anisotropic GDL, (a-ii) liquid pressure contour for the isotropic GDL, (b-i) liquid velocity vector for the anisotropic GDL, and (b-ii) liquid velocity vector for the isotropic GDL.

$$\rho_{\mathrm{gas}} \mathbf{u}_{\mathrm{gas}} = \frac{I}{4F}(2M_{\mathrm{H_2O}} - M_{\mathrm{O_2}}) = \frac{I}{2F} M_{\mathrm{H_2}} \qquad [40]$$

Because water and oxygen fluxes are in different directions, the resulting velocity becomes small. However in two phase region, the phase velocities can be approximated as

$$\rho_{\mathrm{gas}} \mathbf{u}_{\mathrm{gas}} = \mathbf{j}_{\mathrm{O_2}} M_{\mathrm{O_2}} = -\frac{I}{4F} M_{\mathrm{O_2}} \qquad [41]$$

$$\rho_{\mathrm{liq}} \mathbf{u}_{\mathrm{liq}} = \mathbf{j}_{\mathrm{H_2O}} M_{\mathrm{H_2O}} = \frac{I}{2F}(1 + 2\alpha) M_{\mathrm{H_2O}} \qquad [42]$$

Because water and oxygen do not share the same velocity field anymore, the phases are separated and the gas velocity is significantly higher in the two-phase regions.

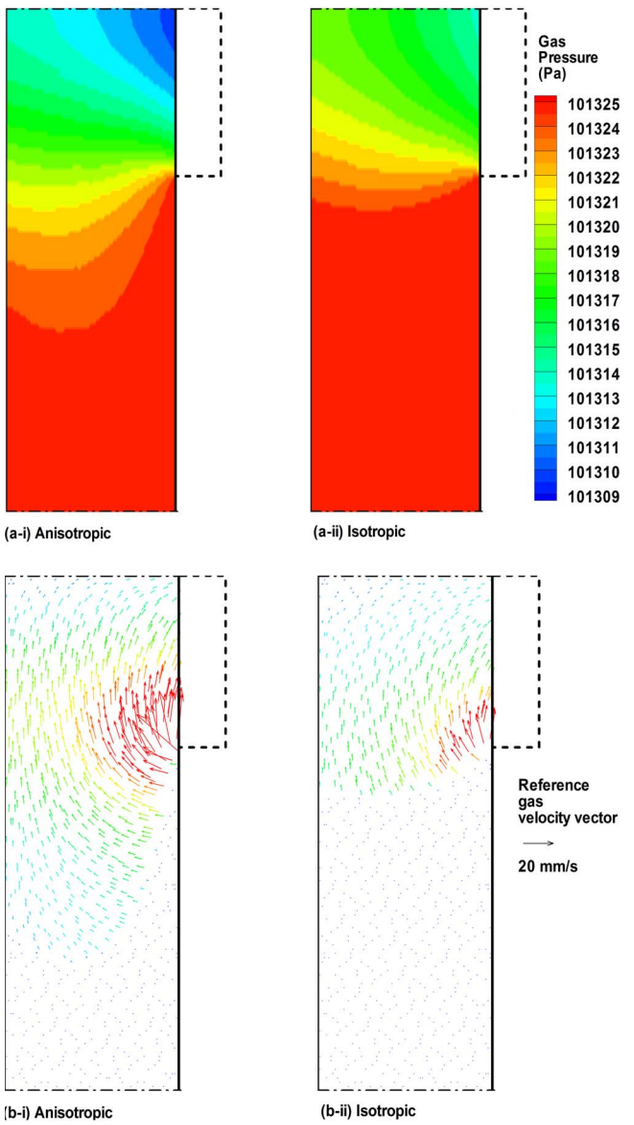

Figure 14. (Color online) Pressure contours and velocity vectors at 0.4 V cell voltage pertaining to the gas flow-field for both the isotropic and anisotropic GDLs. (a-i) Gas pressure contour for the anisotrop GDL, (a-ii) gas pressure contour for the isotropic GDL, (b-i) gas velocity vector for the anisotropic GDL, and (b-ii) gas velocity vector for the isotropic GDL.

Figure 13 and 14 clearly show that the M^2 model is not a homogenous mixture model, rather a reformulation of the two-fluid model, capable of resolving the flow-fields for both phases individually.

Conclusions

A two-dimensional model for predicting the two-phase transport of heat and water was developed and applied to investigate the temperature and water distributions in the cross section of the cathode GDL in a PEFC. The main focus was to assess the effect of anisotropy of the gas diffusion layer on the coupled heat and mass transport in the cathode. The following conclusions are drawn from this study.

Depending on the anisotropy of the GDL and the cell voltage, a temperature differential of up to 5°C is predicted by the model. The fibrous structure of the GDL results in inherently higher conductivities along the fiber directions (i.e., usually the in-plane direction), and this anisotropy strongly affects the temperature distribution. The assumption of the isotropic conductivity for GDL fails to predict the temperature distribution accurately.

The temperature distribution strongly affects the two-phase transport of water. Different temperature profiles are predicted for anisotropic and isotropic GDLs as a result of different thermal conductivities in the in-plane direction. This strongly affects the water transport and results in significantly different liquid saturation distributions. Due to overall lower temperature predicted, average liquid saturation is higher in the anisotropic GDL.

In the nonisothermal two-phase zone, water removal is by both capillary transport of liquid water and gas phase diffusion of water vapor. The two transport mechanisms aid each other in the through-plane direction across the GDL thickness, but oppose each other in the in-plane direction, i.e., from channel to land.

The present study demonstrates a strong need for coupled, anisotropic two-phase heat and water transport modeling of PEFCs. Work is ongoing to integrate the present anisotropic, nonisothermal, two-phase GDL model into a full-cell PEFC model to capture more profound effects of the temperature distribution on other physicochemical processes in PEFCs, such as the electrochemical kinetics in catalyst layers and hydration of the membrane.

Acknowledgments

U.P. acknowledges helpful discussions with Dr. Shaoping Li of Fluent Inc. for numerical implementation of anisotropic diffusion. Support for this work by Sandia National Laboratories is gratefully acknowledged. Sandia is a multiprogram laboratory operated by Sandia Corporation, a Lockheed Martin Company, for the United States Department of Energy's National Nuclear Security Administration under contract no. DE-AC04-94AL85000.

The University of Connecticut assisted in meeting the publication costs of this article.

Appendix

Orthotropic Diffusion

In an anisotropic media, the diffusion flux of a scalar ϕ in direction i depends not only the gradient of scalar ϕ in direction i, but in other directions, j via

$$-\frac{\partial \phi}{\partial x_i} = \sum_j \frac{1}{\Gamma_{ij}} j_j^{\phi} \qquad [A\text{-}1]$$

where Γ_{ij} is the diffusion coefficient tensor and j_j^{ϕ} is the diffusive flux of scalar ϕ in j direction. This equation can be rewritten for diffusive fluxes as

$$j_i = -\sum_j \Gamma_{ij} \frac{\partial \phi}{\partial x_j} \qquad [A\text{-}2]$$

In an isotropic media, the diffusion tensor contains only diagonal elements (i.e., $\Gamma_{ij} = 0$ when $i \neq j$), therefore the diffusive flux becomes

$$j_i = -\Gamma_i \frac{\partial \phi}{\partial x_i} \qquad [A\text{-}3]$$

For the diffusive flux of scalar ϕ, it can be shown that[42]

$$\sum_i \frac{\partial j_i}{\partial x_i} = \sum_i \frac{\partial}{\partial x_i}\left[\sum_j \Gamma_{ij} \frac{\partial \phi}{\partial x_j}\right] = 0 \qquad [A\text{-}4]$$

Through a suitable transformation, Eq. A-4 is reduced to the canonical form

$$\sum_i \frac{\partial}{\partial \zeta_i}\left[\Gamma_i \frac{\partial \phi}{\partial \zeta_i}\right] = 0 \qquad [A\text{-}5]$$

The transformed coordinates that satisfy Eq. A-5 are called the principal directions of the diffusion media. Consequently, if the principal directions of diffusion media (i.e., directions of the fiber orientation) coincide with the coordinate axes (i.e., orthotropic diffusion), then the diffusive flux of scalar ϕ can be written as

$$j_i = -\Gamma_i \frac{\partial \phi}{\partial x_i} \qquad [A\text{-}6]$$

where $\Gamma_i = \Gamma_{ii}$. The diffusion coefficient tensor, then, reduces to a diagonal tensor

$$\Gamma = \begin{bmatrix} \Gamma_{xx} & 0 & 0 \\ 0 & \Gamma_{yy} & 0 \\ 0 & 0 & \Gamma_{zz} \end{bmatrix} \qquad [A\text{-}7]$$

List of Symbols

C^i	molar concentration of species i, mol/m^3
c_p	specific heat, J/kg K
D^i	diffusion coefficient of species i, m^2/s
F	Faraday's constant, 96487 C/mol
h_{fg}	latent heat of evaporation of water, kJ/kg
I	current density,A/m^2
$\vec{j}_k$	mass flux of phase k, kg/m^2 s
K	absolute permeability, m^2
k	thermal conductivity, W/m K
mf_k^i	mass fraction of species i in phase k
M^i	molecular weight of species i, kg/mol
p	Pressure, Pa
R	universal gas constant, 8.314 J/mol K
s	liquid saturation
U_{oc}	open-circuit potential, V
$\vec{u}$	velocity, m/s
V_{cell}	cell voltage, V

Greek

ε	bulk porosity
γ_c	advection coefficient
η	overpotential [V]
μ	dynamic viscosity, Pa s
ν	kinematic viscosity, m^2/s
ρ	density, kg/m^3
τ	Bruggman correction factor

Subscripts

g	gas
l	liquid
sat	saturation

References

1. C. Y. Wang, *Chem. Rev. (Washington, D.C.)*, **104**, 4727 (2004).
2. H. Ju, H. Meng, and C. Y. Wang, *Int. J. Heat Mass Transfer*, **48**, 1303 (2005).
3. T. V. Nguyen and R. E. White, *J. Electrochem. Soc.*, **140**, 2178 (1993).
4. T. F. Fuller and J. Newman, *J. Electrochem. Soc.*, **140**, 1218 (1993).
5. J. S. Yi and T. V. Nguyen, *J. Electrochem. Soc.*, **145**, 1149 (1998).
6. G. Maggio, V. Recupero, and C. Mantegazza, *J. Power Sources*, **62**, 167 (1996).
7. S. Shimpalee and S. Dutta, *Numer. Heat Transfer, Part A*, **38**, 111 (2000).
8. T. Zhou and H. Liu, *Int. J. Transp. Phenom.*, **3**, 177 (2001).
9. R. Bradean, K. Promislow, and B. Wetton, *Numer. Heat Transfer, Part A*, **42**, 121 (2002).
10. Z. H. Wang, C. Y. Wang, and K. S. Chen, *J. Power Sources*, **94**, 40 (2001).
11. D. Natarajan and T. V. Nguyen, *J. Electrochem. Soc.*, **148**, 1324 (2001).
12. L. You and H. Liu, *Int. J. Heat Mass Transfer*, **45**, 2277 (2002).
13. C. Y. Wang, in *Handbook of Fuel Cells – Fundamentals, Technology and Applications*, Vol. 3, W. Lietsich, A. Lamm, and H. A. Gasteiger, Editors, p. 337, John Wiley & Sons, Chicester (2003).
14. A. Z. Weber, R. M. Darling, and J. Newman, *J. Electrochem. Soc.*, **151**, A1715 (2004).
15. U. Pasaogullari and C. Y. Wang, *J. Electrochem. Soc.*, **151**, A399 (2004).
16. U. Pasaogullari and C. Y. Wang, *Electrochim. Acta*, **49**, 4359 (2004).
17. U. Pasaogullari and C. Y. Wang, *J. Electrochem. Soc.*, **152**, A380 (2005).
18. U. Pasaogullari, C. Y. Wang, and K. S. Chen, *J. Electrochem. Soc.*, **152**, A1574 (2005).
19. A. Z. Weber and J. Newman, *J. Electrochem. Soc.*, **152**, A677 (2005).
20. H. Meng and C. Y. Wang, *J. Electrochem. Soc.*, **152**, 1733 (2005).
21. J.-H. Nam and M. Kaviany, *Int. J. Heat Mass Transfer*, **46**, 4595 (2003).
22. A. Rowe and X. Li, *J. Power Sources*, **102**, 82 (2001).
23. J. Yuan and B. Sunden, *Electrochim. Acta*, **50**, 677 (2004).
24. P. Costamagna, *Chem. Eng. Sci.*, **56**, 323 (2001).
25. T. Berning and N. Djlali, *J. Electrochem. Soc.*, **150**, A1589 (2003).
26. S. Mazumder and J. V. Cole, *J. Electrochem. Soc.*, **150**, A1510 (2003).
27. R. Bradean, K. Promislow, and B. Wetton, in *Proceedings of IMECE04*, 2004 International Mechanical Engineering Congress and Exposition, Anaheim, CA, Nov 13–19, 2004.
28. C. Y. Wang and P. Cheng, *Int. J. Heat Mass Transfer*, **39**, 3607 (1996).
29. E. Birgersson, M. Noponen, and M. Vynnycky, *J. Electrochem. Soc.*, **152**, A1021 (2005).
30. S. M. Senn and D. Poulikakos, *J. Heat Transfer*, **127**, 1245 (2005).
31. Y. Wang and C. Y. Wang, *J. Electrochem. Soc.*, **153**, A1193 (2006).
32. P. W. Atkins, *Physical Chemistry*, 6th ed., W. H. Freeman and Company, New York (1998).
33. M. M. Tomadakis and S. V. Sotirchos, *AIChE J.*, **39**, 397 (1993).
34. K. S. Udell, *Int. J. Heat Mass Transfer*, **28**, 485 (1985).
35. M. V. Williams, E. Begg, L. Bonville, H. R. Kunz, and J. M. Fenton, *J. Electrochem. Soc.*, **151**, A1173 (2004).
36. M. J. Bluemle, V. Gurau, J. A. Mann, Jr., T. A. Zawodzinski, Jr., E. S. De Castro and Y. M. Tsou, Paper 1932 presented at The Electrochemical Society Meeting, Honolulu, HI, Oct 2–8, 2004.
37. Toray Carbon Fiber Paper "TGP-H" Property Sheet, Toray Industries Inc.
38. F. Liu, G. Lu, and C. Y. Wang, *J. Membr. Sci.*, **287**, 126 (2007).
39. F. P. Incropera and D. P. Dewitt, *Fundamentals of Heat and Mass Transfer*, John Wiley and Sons, New York, 1996.
40. S. V. Patankar, *Numerical Heat Transfer and Fluid Flow*, Hemisphere, Washington, DC (1980).
41. Fluent 6.2 User's Guide, Fluent Inc., NH, USA.
42. A. Bejan, *Advanced Engineering Thermodynamics*, 2nd ed. Wiley, New York (1997).
43. http://webbook.nist.gov
44. C. R. Wilke, *J. Phys. Chem.*, **18**, 517 (1950).
45. R. B. Bird, W. E. Stewart, and E. N. Lightfoot, *Transport Phenomena*, Wiley, New York (1960).